PAPER

Check for updates

Tuning the Fe–N₄ sites by introducing Bi–O bonds in a Fe–N–C system for promoting the oxygen reduction reaction†

Huihui Jin,‡[ab] Jiawei Zhu,‡[bc] Ruohan Yu,[b] Wenqiang Li, [iD][d] Pengxia Ji,[b] Lvhan Liang,[b] Bingshuai Liu,[b] Chenxi Hu,[b] Daping He [iD] *[ab] and Shichun Mu [iD] *[bc]

Elemental Bi is effective in optimizing the electrocatalytic activity of perovskite oxides and noble metals, but has never been used to adjust the oxygen reduction activity of Fe/N–C catalysts. Here, in order to introduce the Bi element into the Fe/N–C system with atomic-level dispersion, by means of a rod-like C₃N₄ template carrying Fe and Bi atoms as a sacrificial agent, we successfully dope Bi atoms into the ZIF-8 derived Fe/N–C carbon system with a porous rod-like structure in the form of Bi–O (Fe/Bi-RNC). Mössbauer spectroscopy and electron paramagnetic resonance tests prove that Bi doping leads to the formation of higher active Fe–N sites in Fe/Bi-RNC. The oxygen reduction reaction (ORR) of the as-prepared Fe/Bi-RNC is highly superior to the catalyst without Bi doping (Fe-RNC) in both alkaline and acidic electrolytes. The density functional theory (DFT) calculation results further unveil that the existence of the Bi–O bond reduces the band gap of Fe–N₄, and their cooperation is very favorable for electron transfer in the ORR rate-determining step, thereby triggering excellent oxygen reduction performance. These findings demonstrate that Bi atoms have a facilitating role in Fe/N–C oxygen reduction catalysts.

Introduction

The oxygen reduction reaction (ORR) is closely related to human production and life, and some important energy conversion devices, especially fuel cells and metal–air batteries, need the participation of the ORR.[1,2] However, the ORR occurring on the electrode requires a large amount of precious Pt-based catalysts, which seriously hinders the development of such electrochemical devices.[3,4] Therefore, research on non-precious metal ORR catalysts is imminent. Non-precious metal ORR catalysts are all-encompassing, including transition metal nanoparticles, transition metal carbides, transition metal nitrides, transition metal oxides and metal/N–C series materials,[5–10] in which the outstanding Fe/N–C electrocatalyst is highly sought after, and researchers have done a lot of work on their preparation and modification.[11–14] In particular, heteroatom (such as N, S, P, and B) doping and electronic regulation are considered to be

effective strategies for optimizing the catalyst performance.[15–19] Despite numerous heteroatomic adjustments, no one has ever attempted to adjust the ORR performance by doping bismuth (Bi) atoms in non-noble ORR catalysts.

Hitherto, Bi-based materials such as the Bi-based oxide, Bi₂O₃ as a representative, have been selected as potential electrolyte materials for solid oxide fuel cells (SOFCs) because of their extremely high oxygen ion conductivity.[20–22] Meanwhile, Bi ions with 6s lone electron pairs acting as the A-site component of the perovskite (the cathode catalyst of SOFCs) can increase the overall oxygen vacancy mobility of the catalyst, which leads to the ORR process being more likely to be carried out in the four-electron pathway.[23–26] In addition, elemental Bi also has attractive applications in noble metal catalysts towards proton exchange membrane fuel cells (PEMFCs). Among them the more mature ones are Pt(Pd)Bi alloys.[27–29] In the early days, researchers found that PtBi alloys have excellent methanol/formic acid oxidation properties, owing to the addition of Bi increasing the resistance of Pt catalysts to carbon monoxide. In the later stage, through the directional control of the composition, morphology and structure of PtBi alloys, they exhibited superior ORR performance to commercial Pt/C.[30,31] Guo's group has designed a kind of hcp-PtBi/fcc-Pt core/shell nanoplate for the ORR, whose mass activity was twice that of commercial Pt/C.[32] And DFT calculation showed that the outstanding ORR performance was attributed to the existence of the Bi-p empty band weakening the excessive bonding of O on the Pt shell of the hcp-PtBi/fcc-Pt core/shell nanoplate. Recently, Hall's group

[a]Hubei Engineering Research Center of RF-Microwave Technology and Application, Wuhan University of Technology, Wuhan 430070, China. E-mail: hedaping@whut.edu.cn; msc@whut.edu.cn

[b]State Key Laboratory of Advanced Technology for Materials Synthesis and Processing, Wuhan University of Technology, Wuhan 430070, China

[c]Foshan Xianhu Laboratory, Foshan 528200, China

[d]Henan Key Laboratory of Function-Oriented Porous Materials, College of Chemistry and Chemical Engineering, Luoyang Normal University, Luoyang 471934, China

† Electronic supplementary information (ESI) available: Experimental details and supplementary figures and tables. See DOI: 10.1039/d1ta08256f

‡ These authors contributed equally to this work.

synthesized $Pd_{31}Bi_{12}$ nanoparticles with superior ORR performance.[33] Compared with Pt/C, the mass activity of the obtained $Pd_{31}Bi_{12}$ nanoparticles was increased by 7 times, and compared with Pd/C, the mass activity was increased by 4 times. Since the Bi element has been well-established in perovskites and noble metals, it is worthwhile to explore whether Bi atoms would benefit the ORR performance of the Fe/N–C system.

To introduce Bi atoms into the carbon structure derived from ZIF-8, C_3N_4 with rich nitrogen sources and susceptible to decomposition at high temperatures (>700 °C)[34,35] is selected as a sacrificial intermediate template agent. Here, by introducing Fe and Bi atoms into the C_3N_4 structure, and then combining with ZIF-8, Fe and Bi atoms are transferred into the carbon structure derived from ZIF-8 at 900 °C with the sacrifice of C_3N_4, and finally rod-like porous carbon materials with Fe and Bi are obtained (Fe/Bi-RNC). The experimental results reveal that the Fe and Bi co-doped carbon material possesses superior ORR performance to the only Fe-doped carbon material in both alkaline and acidic electrolytes. Bi is observed by X-ray photoelectron spectroscopy (XPS) analysis in the form of the Bi–O bond in the Fe/Bi-RNC structure, which is capable of enhancing the ORR dynamics of Fe–N_4, as proved by the Fe Mössbauer spectroscopy and DFT calculation analysis.

Experimental

Synthesis of catalysts

Preparation of Fe/Bi–C_3N_4. 1 g of melamine was dispersed in 20 mL of ethylene glycol, 0.136 g of $Fe(NO_3)_3 \cdot 9H_2O$ and 0.240 g of $Bi(NO_3)_3 \cdot 5H_2O$ were dissolved in 0.15 M HNO_3 solution, and then the metal salt solution was slowly dropped into the ethylene glycol solution. After stirring for 1 h, the suspension was centrifuged, washed three times, and dried in a 60 °C vacuum oven for 12 h. The obtained powder was placed in a tube furnace and annealed at 450 °C for 2 h in a N_2 atmosphere, and the product was named Fe/Bi–C_3N_4. Under the same synthesis conditions, Fe–C_3N_4 was synthesized without $Bi(NO_3)_3 \cdot 5H_2O$, and C_3N_4 was synthesized without metal salts.

Preparation of Fe/Bi–C_3N_4@ZIF. 300 mg Fe/Bi–C_3N_4, 1.2 g $Zn(NO_3)_2 \cdot 6H_2O$ and 600 mg polyvinylpyrrolidone (PVP, K30) were dispersed in 36 mL of methanol and sonicated for 1 h. 2.649 g 2-methylimidazole was dissolved in 36 mL of methanol, then added to the salt solution, and stirred for 4 h. The obtained product was centrifuged and washed with methanol 3 times, dried in a 60 °C vacuum oven for 12 h, and was named Fe/Bi–C_3N_4@ZIF. Under the same synthesis conditions, Fe–C_3N_4@ZIF was synthesized with Fe–C_3N_4, C_3N_4@ZIF was synthesized with C_3N_4, and ZIF-8 was synthesized without C_3N_4.

Preparation of Fe/Bi-RNC. Fe/Bi–C_3N_4@ZIF was calcined at 900 °C for 3 h under N_2 protection, and after naturally cooling to room temperature, the obtained sample was named Fe/Bi-RNC. Under the same temperature conditions, Fe-RNC was derived from Fe–C_3N_4@ZIF, RNC was derived from C_3N_4@ZIF, and NC was derived from ZIF-8. Fe/Bi_L-RNC was synthesized with 0.120 g of $Bi(NO_3)_3 \cdot 5H_2O$ and Fe/Bi_M-RNC was synthesized with 0.360 g of $Bi(NO_3)_3 \cdot 5H_2O$. Additionally, Fe_L-RNC and Fe_M-RNC were

prepared for comparison, using 0.068 g $Fe(NO_3)_3 \cdot 9H_2O$ and 0.244 g $Fe(NO_3)_3 \cdot 9H_2O$, respectively.

Fabrication of the primary zinc–air battery

Liquid zinc–air battery. The liquid zinc–air battery is composed of polished zinc foil as the anode, carbon paper coated with the catalyst (1 mg cm^{-2}) as the cathode, and 6 M KOH and 0.2 M $Zn(CH_3COO)_2$ mixed solution as the electrolyte.

All solid-state zinc–air battery. The all solid-state zinc–air battery is composed of a polished zinc sheet as the anode, nickel mesh containing the catalyst as the cathode and polyvinyl alcohol (PVA) film containing KOH and $Zn(CH_3COO)_2$ as the solid electrolyte. The preparation of the PVA membrane was as follows: 5 g PVA powder, 0.297 g KOH and 0.165 g $Zn(CH_3COO)_2$ were added to 50 mL deionized water, then stirred at 90 °C to form a transparent gel, and finally spread it into a film in a Petri dish and froze in a refrigerator.

Results and discussion

Morphology and structural characterization

The preparation of the porous rod-like carbon material (Fe/Bi-RNC) doped with iron (Fe) and bismuth (Bi) is divided into three steps (Fig. 1a). First was the synthesis of a rod-like C_3N_4 template containing Fe and Bi atoms (Fe/Bi–C_3N_4). The specific preparation method is shown in the Experimental section. The Fe/Bi–C_3N_4 template as a micron-sized rod-shaped product was the result of melamine undergoing hydrolysis, protonation and low-temperature pyrolysis. Second, the prepared C_3N_4 template was dispersed in a methanol solution containing $Zn(NO_3)_2 \cdot 6H_2O$ and polyvinylpyrrolidone (PVP), then stirred with 2-methylimidazole methanol solution for 4 h to obtain a precursor (Fe/Bi–C_3N_4@ZIF) assembled from ZIF-8 and C_3N_4, as suggested by their XRD patterns (Fig. S1†). Finally, Fe/Bi–C_3N_4@ZIF was maintained at 900 °C for 3 h in a N_2 atmosphere to obtain Fe/Bi-RNC. During pyrolysis, Fe/Bi–C_3N_4 was completely decomposed at 900 °C and released Fe and Bi atoms into the ZIF-8-derived carbon material, but the rod morphology did not collapse with the decomposition of C_3N_4 on account of the presence of the strong binder PVP in the precursor. Thus, a Fe, Bi-doped porous rod-like carbon material (Fe/Bi-RNC) was obtained. The same method was used for the preparation of Fe-RNC and RNC without using $Bi(NO_3)_3 \cdot 5H_2O$ or metal salts, respectively. NC was derived from ZIF-8.

From SEM and TEM images (Fig. 1b, S2 and S3†), the as-obtained Fe/Bi-RNC still maintains a micron-level rod-like structure, but with a rugged surface, and the complete polyhedral carbon matrix cannot be observed on the Fe/Bi-RNC surface. On the one hand, the cyanide fragments produced by the decomposition of C_3N_4 at high temperatures would react with carbon, thus eroding the polyhedron carbon derived from ZIF-8 on the outer surface of the rod. On the other hand, the gas produced by the decomposition of C_3N_4 and PVP was constantly released from the inside, continuously attacking the outer carbon structure. Combining these two reasons, the Fe/Bi-RNC surface cannot display a regular morphology which leads to the relatively loose
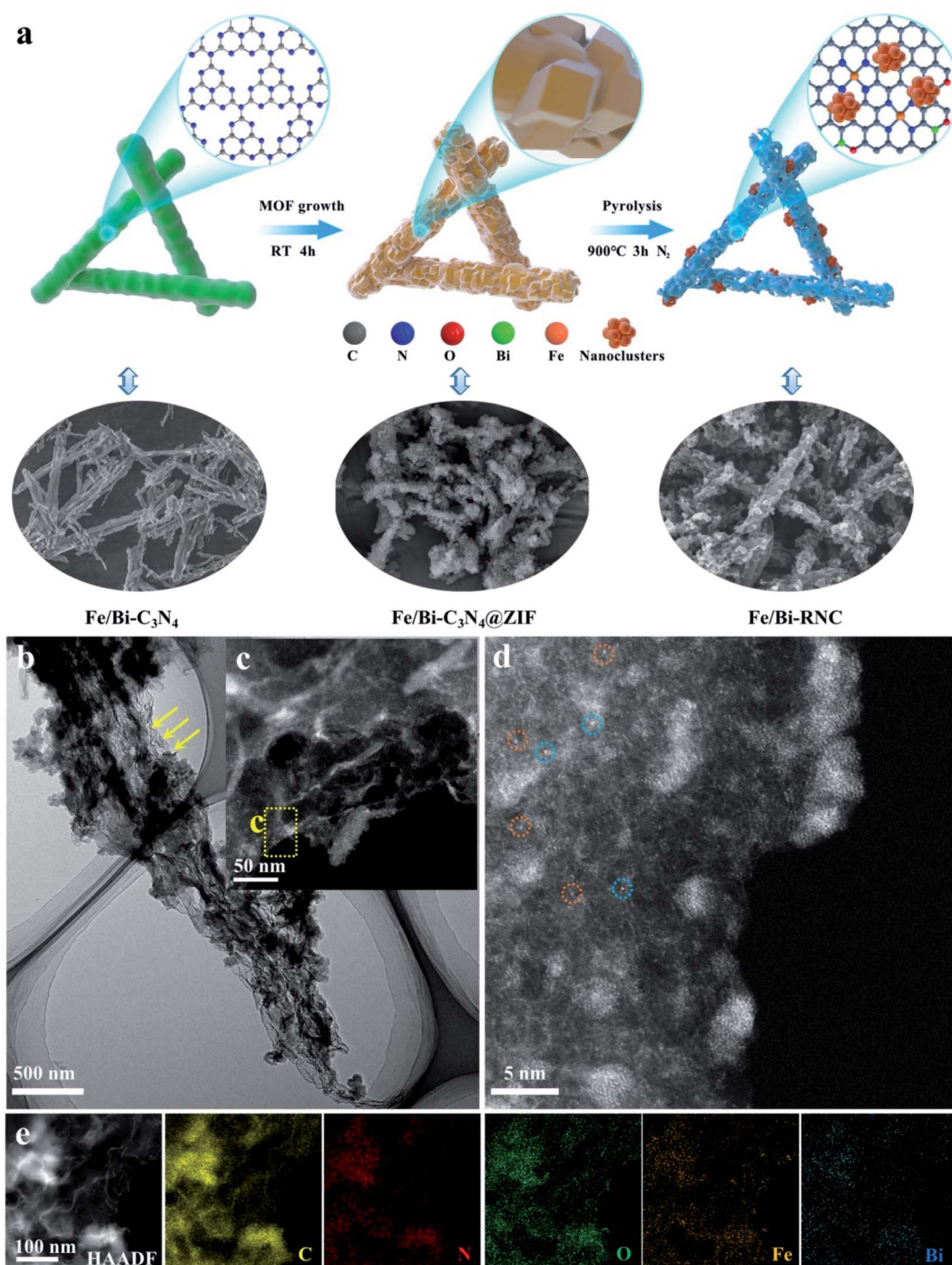
Fig. 1 (a) Preparation process of Fe/Bi-RNC; microscopic morphology characterization of Fe/Bi-RNC. (b) TEM, (c) HRTEM, (d) AC HAADF-STEM (yellow circles: Fe atoms and blue circles: Bi atoms), and (e) EDS mapping images.

carbon skeleton with an obvious pore structure (Fig. 1b and c). Dramatically, the AC HAADF-STEM image shows that some atoms exhibit a bright spot distribution due to their atomic-level dispersion (Fig. 1d). Owing to the higher atomic number of the Bi element than the Fe element in the periodic table, the Bi atoms obviously present a brighter state when the metal atoms are dispersed at the atomic level. As shown in Fig. 1d, Bi atoms are marked with blue circles, and Fe atoms are marked with yellow

circles. Also, elemental mapping images verify that Fe and Bi atoms have been successfully doped into the carbon structure through the decomposition of C_3N_4 (Fig. 1e). And because of the uniform distribution of metal atoms, no metal species are observed in the XRD patterns of Fe/Bi-RNC and Fe-RNC (Fig. S4†), with only two broad carbon peaks representing graphite carbon (002) and amorphous carbon (100).

Fig. 2a shows the N_2 absorption/desorption test results, and compared with original NC, Fe-RNC and Fe/Bi-RNC have obvious hysteresis loops as a consequence of more mesopores in the product. Moreover, the fluctuating data points in the range of 5–30 nm in the pore size distribution plot of the sample prepared with C_3N_4 exactly confirm the irregular mesopores caused by the decomposition of C_3N_4 (Fig. 2b), corresponding to the TEM image in Fig. 1c. Fortunately, appropriate mesopores are highly beneficial for exposing more active sites and facilitate remote mass transfer.[36,37] Although the products prepared with C_3N_4 as the sacrificial template have more mesopores, in Raman spectra (Fig. S5†), the I_D/I_G values of NC, Fe-RNC and Fe/Bi-RNC are almost the same (D refers to the carbon defects and is located at 1300 cm^{-1} and G refers to the graphitization of carbon and is located at 1580 cm^{-1}),[38] indicating that no more defects are produced in the product prepared with C_3N_4.

In Fig. 2c, the state of elemental Bi in Fe/Bi-RNC is shown in the high-resolution Bi 4f XPS, which can be divided into Bi $4f_{7/2}$ (159.0 ± 0.1 eV) and Bi $4f_{5/2}$ (164.3 ± 0.1 eV), indicating that Bi is bound to O in the carbon structure.[39,40] Meanwhile, FTIR spectra also confirm the presence of Bi–O bonds in Fe/Bi-RNC with the vibration peaks located around 560 cm^{-1} and 850–900 cm^{-1} (Fig. S6†).[41] Subsequently, Fe Mössbauer spectroscopy was performed to reveal the coordination state of Fe in the sample and the effect of Bi–O bonds on the Fe structure. After comparing with the literature, it can be concluded that D1, D2 and D3 are attributed to the Fe–N_4 coordination (fitting parameters in Table S1†).[42,43] D1 is Fe(II)–N_4 in the low spin state, D2 is Fe(II)–N_4 similar to $[FePc]^{2-}$, and D3 belongs to Ox-Fe(III)–N_4 (Fig. 2c and d). The appearance of the Ox-Fe(III)–N_4 site in Fe/Bi-RNC may be the effect of the Bi–O bond. Notably, the Ox-Fe(III)–N_4 site plays an important role in oxygen reduction. Meanwhile, the EPR spectra of Fe show that Fe/Bi-RNC has

a higher G value (Fig. 2e), which may be the influence of the Bi–O bond with the high electron withdrawing effect on Fe sites in Fe/Bi-RNC, thereby regulating the Fe–N_4 site and benefiting the subsequent oxygen reduction.[15,44]

Since C_3N_4 is rich in nitrogen sources, it undoubtedly produces changes in the N type of the product prepared with C_3N_4 in addition to providing N. Fig. S7† shows the N 1s high-resolution XPS spectra of NC, RNC, Fe-RNC and Fe/Bi-RNC, and three types of N peaks (pyridinic N, pyrrolic N and graphitic N) can be obtained by peak fitting, located at 398 eV, 400 eV and 401 eV, respectively. More importantly, the relative proportion of graphitic N in the sample prepared with C_3N_4 is significantly higher than that in original NC (Fig. S8†), and thus is conducive to the improvement of ORR activity.[45,46]

Oxygen reduction reaction performance

Immediately, the effect of Bi atoms on the electrocatalytic performance of oxygen reduction was explored. Fig. 3a shows the typical oxygen reduction curves measured by LSV in 0.1 M KOH. The onset potential (E_{onset}) and half-wave potential ($E_{1/2}$) of each catalyst are summarized in Fig. S9.† The original NC has an E_{onset} of 0.875 V and an $E_{1/2}$ of 0.773 V. After being combined with the C_3N_4 template, the E_{onset} (0.885 V) and $E_{1/2}$ (0.783 V) of the as-prepared rod-like RNC catalyst are improved. Apparently, benefiting from its porous rod-like structure, RNC not only exposes a large number of active sites, but also facilitates charge transport. Simultaneously, additional nitrogen doping is also propitious to improve the ORR kinetics of carbon materials. Then, by further doping with Fe atoms, the ORR activity (E_{onset} and $E_{1/2}$) of the Fe-RNC catalyst is greatly enhanced, and its $E_{1/2}$ (0.861 V) has exceeded that of 20% Pt/C (0.854 V). Surprisingly,
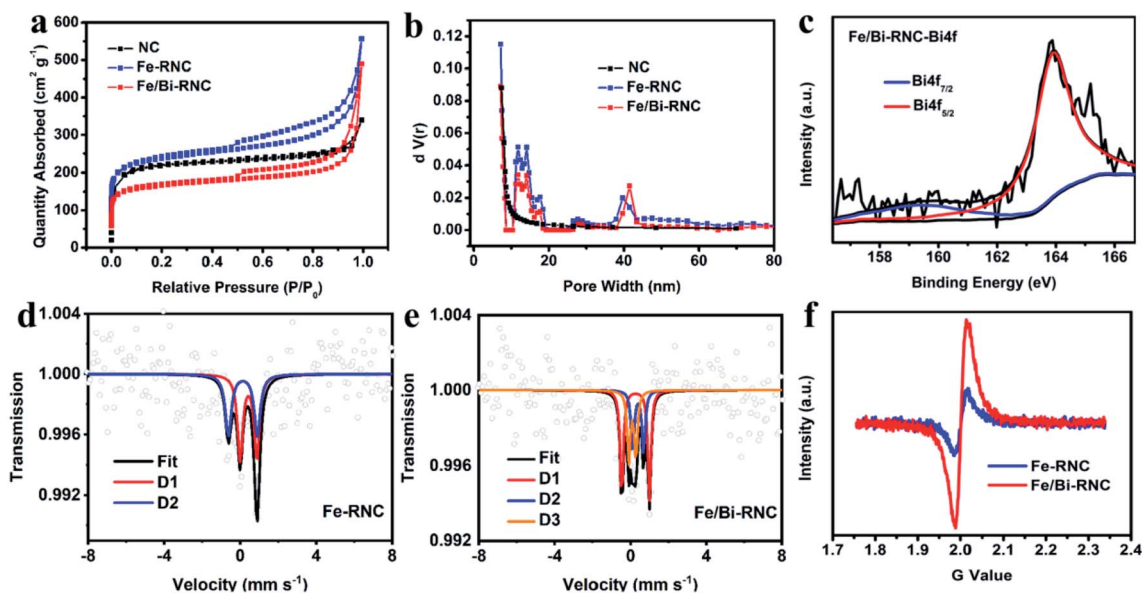

Fig. 2 Structural characterization. (a) N_2 sorption isotherms and (b) pore-size distribution of NC, Fe-RNC and Fe/Bi-RNC, (c) Bi 4f XPS of Fe/Bi-RNC, (d) Fe Mössbauer spectroscopy of Fe-RNC, (e) Fe Mössbauer spectroscopy of Fe/Bi-RNC, and (f) Fe EPR of Fe-RNC and Fe/Bi-RNC.
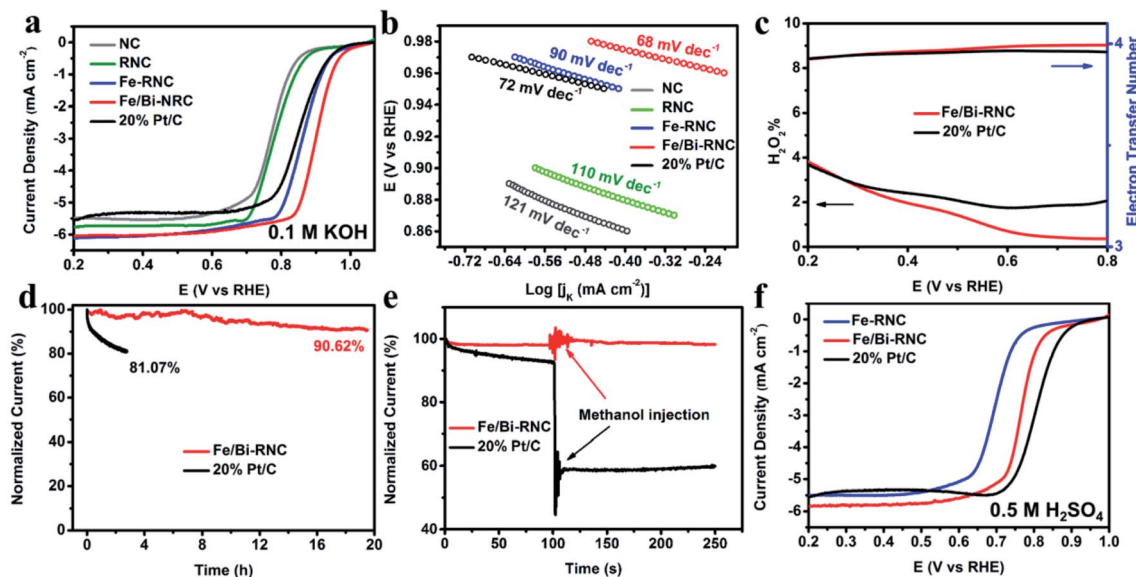
This journal is © The Royal Society of Chemistry 2022

J. Mater. Chem. A, 2022, **10**, 664–671 | **667**

Fig. 3 Oxygen reduction performance test. (a) LSV curves in O_2-saturated 0.1 M KOH, (b) Tafel slope, (c) H_2O_2 yield and electron transfer number, (d) stability test, (e) methanol tolerance test, and (f) LSV curves in O_2-saturated 0.5 M H_2SO_4.

the oxygen reduction activity does not change much in different iron doped samples (Fe_L-RNC, Fe-RNC, and Fe_M-RNC), but all the catalysts (Fe/Bi_L-RNC, Fe/Bi-RNC, and Fe/Bi_M-RNC) prepared by doping different amounts of Bi atoms into Fe-RNC present better ORR activity. Although the oxygen reduction activity of Fe/Bi-RNC series samples does not increase with the increase of Bi dopants, the positive effect of Bi doping on the oxygen reduction activity of the samples is significantly higher than the change in Fe doping compared to the Fe-RNC series samples (Fig. S10 and Table S2†). Among them, the most superior active Fe/Bi-RNC catalyst has an $E_{1/2}$ of 0.899 V higher than that of Fe-RNC by 38 mV, and also better than most Fe-based non-noble metal oxygen reduction catalysts (Table S3†), indicating that the doping of Bi atoms successfully promotes the oxygen reduction ability of the active site. In addition, the Tafel slope (Fig. 3b) shows that all samples follow the second electron transfer as the rate-determining step,[47] where Fe/Bi-RNC with the smallest Tafel slope manifests its most excellent oxygen reduction ability in the kinetic control region.

Furthermore, in the rotating ring disk electrode (RRDE) test, Fe/Bi-RNC exhibits outstanding ability to oxidize H_2O_2 over commercial Pt/C (Fig. 3c). Coincidentally, the electron transfer number (n) was calculated to be 3.93 (Fig. S11†), reflecting that its ORR process was close to the four-electron pathway. Besides, stability and resistance to methanol are also important indicators to evaluate the practicality of ORR catalysts. As tested, the current of Fe/Bi-RNC attenuates by only 9.38% in constant voltage tests for consecutive 20 h, while commercial Pt/C is unable to maintain the initial activity after 6 h of testing (Fig. 3d). The same situation occurs in methanol tolerance measurements, where methanol can poison commercial Pt/C but is ineffective for Fe/Bi-RNC (Fig. 3e).

To further reflect the superiority of Bi doping, the working electrode coated with Fe/Bi-RNC was continuously measured in

0.5 M H_2SO_4 electrolytes, and compared with Fe-RNC and 20% Pt/C. The ORR activity of Fe/Bi-RNC under acidic conditions is close to that of commercial Pt/C. And as expected, Fe/Bi-RNC still has stronger oxygen reduction ability than Fe-RNC with the half-wave potential exceeding that of Fe-RNC by approximately 70 mV (Fig. 3f and S12†). At the same time, Fe/Bi-RNC has a lower Tafel slope than Fe-RNC, confirming that Fe/Bi-RNC maintains better kinetics under acidic conditions (Fig. S13†). Moreover, only a small amount of H_2O_2 is produced by Fe/Bi-RNC during the ORR process (Fig. S14†), and even comparable to commercial Pt/C, its electron transfer number is almost 4 through the calculation based on the H_2O_2 yield or LSV curves recorded at different rotating speeds (Fig. S15†). Impressively, Fe/Bi-RNC maintains a current of 86.02% even after 20 h of stability testing in an acidic environment, far surpassing the stability of commercial Pt/C (Fig. S16†), and is fully resistant to methanol (Fig. S17†).

Zinc–air battery application

Afterwards, a self-made zinc–air battery was fabricated by using carbon paper coated with Fe/Bi-RNC or commercial Pt/C ink (1 mg cm^{-2}) as the cathode (Fig. 4a). Benefiting from the more positive and stable ORR performance of Fe/Bi-RNC in an alkaline environment than commercial Pt/C, the zinc–air battery with Fe/Bi-RNC as the air electrode exhibits a peak power density of 144 mW cm^{-2}, a discharge voltage of 1.33 V at 5 mA, higher than commercial Pt/C (peak power density: 109 mW cm^{-2} and discharge voltage: 1.28 V at 5 mA) (Fig. 4b and c). In particular, when Fe/Bi-RNC mixed with RuO_2 is used as the cathode, it can realize stable discharge performance (Fig. 4d). And the all-solid-state zinc–air battery constructed with Fe/Bi-RNC reaches an open circuit voltage of 1.41 V (Fig. 4e), so that such three series-connected batteries are fully capable of illuminating three parallel 3 V LEDs, as shown in Fig. 4f.
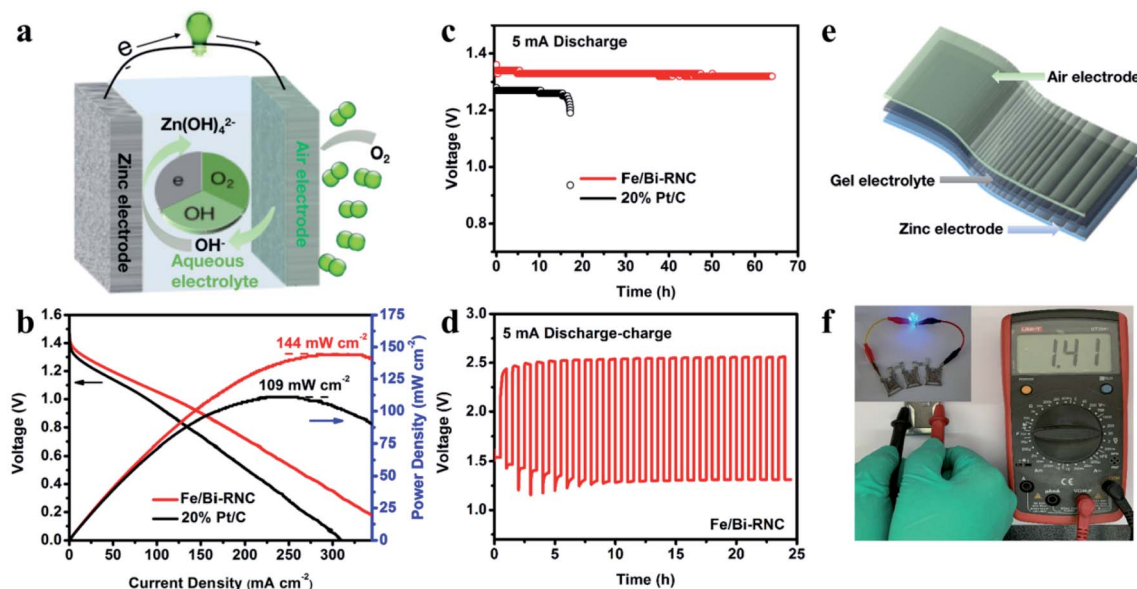
668 | *J. Mater. Chem. A*, 2022, **10**, 664–671

This journal is © The Royal Society of Chemistry 2022

Fig. 4 Zn–air battery. (a) Liquid electrolyte zinc–air battery, (b) polarization curves and (c) discharge performance at 5 mA of Fe/Bi-RNC and 20% Pt/C, (d) long-term discharge–charge curves at 5 mA of Fe/Bi-RNC, (e) all-solid-state zinc–air battery, and (f) pictures of lit LED and open circuit voltage of the battery with Fe/Bi-RNC as the cathode.

DFT calculation

Firstly, KSCN was employed to poison Fe/Bi-RNC during LSV testing and it was found that the ORR activity of Fe/Bi-RNC dramatically decreased after the addition of KSCN (Fig. S18†), indicating that the Fe–N$_x$ site mainly provides ORR activity in Fe/Bi-RNC. Then, to clarify the key role of Bi–O bonds on the isolated Fe–N$_4$ sites, density functional theory (DFT) calculations were

conducted. The theoretical model was built on the basis of the graphene nanoribbon with adjoining edge Bi–O bonds next to the Fe–N$_4$ center (named Fe–N$_4$–BiO). From the construction configuration after the geometry optimization, the graphene plane of Fe–N$_4$–BiO was dragged and became wrinkled, while the simplex Fe–N$_4$ would not change the planarity (Fig. S19†). The surface roughness might also result in the stretching of
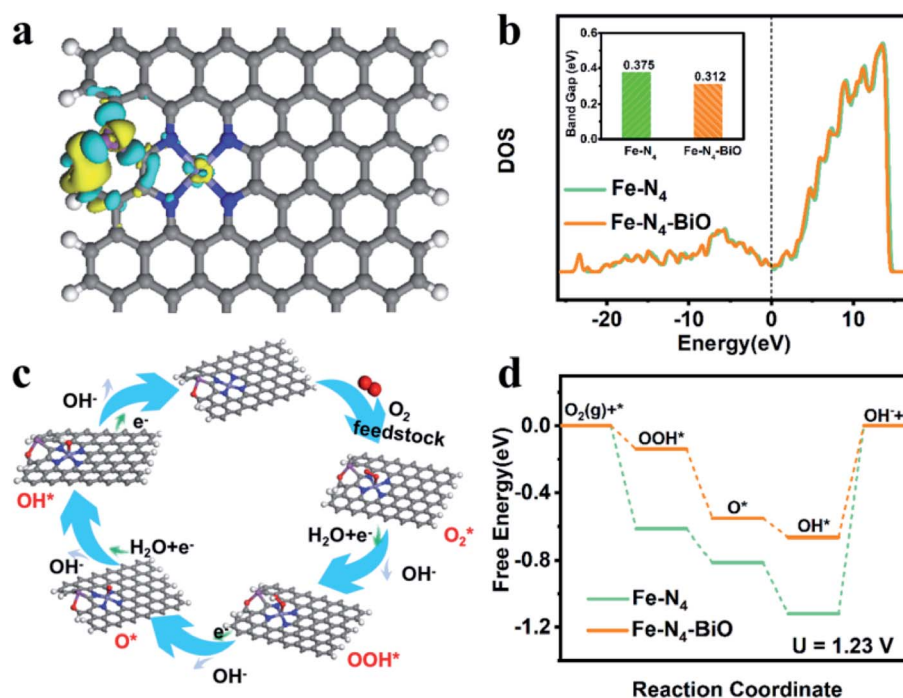

Fig. 5 DFT calculation. (a) Charge density difference of Fe–N$_4$–BiO; (b) density of states and inserted band gap for Fe–N$_4$ and Fe–N$_4$–BiO models; (c) schematic illustration of the proposed ORR pathway; (d) ORR free energy diagram of Fe–N$_4$ and Fe–N$_4$–BiO models.

This journal is © The Royal Society of Chemistry 2022

J. Mater. Chem. A, 2022, **10**, 664–671 | **669**

neighboring Fe–N bond lengths and then modify the electronic structure of central Fe–N_4 sites.[48] The optimized electronic structure was first analyzed by charge density difference. As shown in Fig. 5a, the introduction of edge Bi–O bonds would result in the local charge density redistribution. Importantly, it can also affect the charge density of neighboring central Fe atoms through long-term delocalization, thereby elevating the catalytic activity.[49] The density of states exhibits almost identical shape after introducing Bi–O bonds, indicating the reserved structural integrity (Fig. 5b).[50] Moreover, the reduced band gap of Fe–N_4–BiO signifies that the Bi–O bond doping can effectively modulate the electronic structure and enhance the electron transfer capability. The possible ORR mechanism was proposed, as shown in Fig. 5c. The oxygen adsorption energy was first employed upon both models. This exhibits that Fe–N_4–BiO possesses a stronger adsorption ability than Fe–N_4, suggesting the better catalytic activity (Fig. S20†). Besides, the stretched O–O bond length upon Fe–N_4–BiO is favorable for the bond rupture, therefore initiating the ORR process. As we know, the ORR performance mainly depends on the reaction energy barrier of the rate-determining step; thus, the adsorption behaviors of multiple reaction intermediates upon Fe–N_4 and Fe–N_4–BiO are compared to reveal the internal reaction mechanism. The adsorption configurations are presented in Fig. S21 and S22.† As shown in Fig. 5d, the rate-determining steps for both models are all the last step, namely charging the adsorbed OH* to form OH⁻.[51] And Fe–N_4–BiO is more beneficial for achieving the electron transfer from the synergetic site to the OH* species; therefore, it exhibits a smaller ORR overpotential than the Fe–N_4 site. Differently, the Bi site becomes the adsorption site of the onefold BiO model (Fig. S23†), which is subject to the formation of the OOH* intermediate from adsorbed oxygen with a much larger theoretical overpotential than the Fe–N_4 and Fe–N_4–BiO models. This suggests that the BiO site cannot be the active site for oxygen reduction (Fig. S24†). In brief, the introduction of adjacent Bi–O bonds effectively modifies the electronic structure of the isolated Fe–N_4 sites, optimizes the adsorption behavior of the reaction intermediates, and consequently boosts the ORR performance.

Conclusions

In summary, we successfully designed and constructed a Fe, Bi co-doped carbon material (Fe/Bi-RNC) with a porous rod structure using C_3N_4 as a self-sacrificing template. During the carbonization process, Fe and Bi atoms released by C_3N_4 decomposition are captured by N atoms and O atoms to form Fe–N_4 sites and Bi–O bonds with atom-scale dispersion, respectively. The experimental results show that the as-prepared Fe/Bi-RNC possesses better oxygen reduction performance than Fe-RNC in both acidic and alkaline environments, which is attributed to the promotive effect of Bi–O bonds on the oxygen reduction kinetics of Fe–N_4, as further demonstrated by the DFT calculation results. Therefore, this work is significant for the regulation of Fe/N–C activity and provides a new direction for Bi atoms to promote the oxygen reduction catalytic activities of the Fe/N–C system.

Author contributions

The manuscript was completed through the contributions of all authors. H. H. Jin and J. W. Zhu contributed equally to this work. H. H. Jin, D. P. He and S. C. Mu considered the idea and designed the experiments. J. W. Zhu and W. Q. Li performed the DFT calculations. R. H. Yu and P. X. Ji performed the electron microscope characterization. L. H. Liang, B. S. Liu and C. X. Hu performed the main experiments and analyzed the data.

Conflicts of interest

There are no conflicts to declare.

Notes and references

1 G. G. Yang, J. W. Zhu, P. F. Yuan, Y. F. Hu, G. Qu, B. A. Lu, X. Y. Xue, H. B. Yin, W. Z. Cheng, J. Q. Cheng, W. J. Xu, J. Li, J. S. Hu, S. C. Mu and J. N. Zhang, *Nat. Commun.*, 2021, **12**, 1–10.

2 L. Liu, T. Ma, W. Fang, Y. Liu, K. Konstantinov, J. Wang and H. Liu, *Energy Environ. Mater.*, 2021, **4**, 239–245.

3 M. Mazzucato, G. Daniel, A. Mehmood, T. Kosmala, G. Granozzi, A. Kucernak and C. Durante, *Appl. Catal., B*, 2021, **291**, 120068.

4 L. Liu, G. Zeng, J. Chen, L. Bi, L. Dai and Z. Wen, *Nano Energy*, 2018, **49**, 393–402.

5 M. G. Wang, W. J. Yang, X. Z. Li, Y. S. Xu, L. R. Zheng, C. L. Su and B. Liu, *ACS Energy Lett.*, 2021, **6**, 379–386.

6 S. L. Zhang, B. Y. Guan and X. W. Lou, *Small*, 2019, **15**, 1805324.

7 Y. Yu, J. Zhou and Z. Sun, *Adv. Funct. Mater.*, 2020, **30**, 2000570.

8 X. Tian, X. Lu, B. Xia and X. Lou, *Joule*, 2020, **4**, 45–68.

9 Q. Liu, B. Yu, X. Liao and Y. Zhao, *Energy Environ. Mater.*, 2020, 1–7.

10 K. N. Dinh, Q. H. Liang, C. F. Du, J. Zhao, A. I. YoongTok, H. Mao and Q. Y. Yan, *Nano Today*, 2019, **25**, 99–121.

11 X. Liu, H. Liu, C. Chen, L. L. Zou, Y. Li, Q. Zhang, B. Yang, Z. Q. Zou and H. Yang, *Nano Res.*, 2019, **12**, 1651–1657.

12 H. Yang, X. Chen, W. T. Chen, Q. Wang, N. C. Cuello, A. Nafady, A. M. Al-Enizi, G. I. N. Waterhouse, G. A. Goenaga, T. A. Zawodzinski, P. E. Kruger, J. E. Clements, J. Zhang, H. Tian, S. G. Telfer and S. Q. Ma, *ACS Nano*, 2019, **13**, 8087–8098.

13 X. R. Zhang, Y. B. Mollamahale, D. Lyu, L. Z. Liang, F. Yu, M. Qing, Y. H. Du, X. Y. Zhang, Z. Q. Tian and P. K. Shen, *J. Catal.*, 2019, **372**, 245–257.

670 | *J. Mater. Chem. A*, 2022, **10**, 664–671

This journal is © The Royal Society of Chemistry 2022

14 L. Y. Gong, H. Zhang, Y. Wang, E. G. Luo, K. Li, L. Q. Gao, Y. M. Wang, Z. J. Wu, Z. Jin, J. J. Ge, Z. Jiang, C. P. Liu and X. Wei, *Angew. Chem., Int. Ed.*, 2020, **132**, 14027–14032.

15 Y. Mun, S. Lee, K. Kim, S. Kim, S. Lee, J. W. Han and J. Lee, *J. Am. Chem. Soc.*, 2019, **141**, 6254–6262.

16 M. Wang, H. Ji, S. Liu, H. Sun, J. Liu, C. Yan and T. Qian, *Chem. Eng. J.*, 2020, 124702.

17 B. Ni, R. Chen, L. Wu, X. Xu, C. Shi, P. Sun and T. Chen, *ACS Appl. Mater. Interfaces*, 2020, **12**, 23995–24006.

18 K. Yuan, D. Lützenkirchen-Hecht, L. B. Li, L. Shuai, Y. Z. Li, R. Cao, M. Qiu and X. D. Zhuang, *J. Am. Chem. Soc.*, 2020, **142**, 2404–2412.

19 X. D. Long, Z. L. Li, G. Gao, P. Sun, J. Wang, B. S. Zhang, J. Zhong, Z. Jiang and F. W. Li, *Nat. Commun.*, 2020, **19**, 1215–1223.

20 E. D. Wachsman and K. T. Lee, *Science*, 2011, **334**, 935–939.

21 B. H. Yun, K. J. Kim, D. W. Joh, M. S. Chae, J. J. Lee, D. W. Kim and K. T. Lee, *J. Mater. Chem. A*, 2019, **7**, 20558–20566.

22 R. D. Bayliss, S. N. Cook, S. Kotsantonis, R. J. Chater and J. A. Kilner, *Adv. Energy Mater.*, 2014, **4**, 1301575.

23 Y. Kong, C. Z. Sun, X. Wu, K. N. Sun, X. J. Yin and N. Q. Zhang, *ACS Sustainable Chem. Eng.*, 2020, **8**, 3950–3958.

24 Y. Wang, Y. Xing, Z. Xu, S. Xue, S. Zhang and C. Xia, *Appl. Catal., B*, 2020, **269**, 118809.

25 X. Y. Hu, M. Li, Y. Xie, Y. Yang, X. J. Wu and C. R. Xia, *ACS Appl. Mater. Interfaces*, 2019, **11**, 21593–21602.

26 M. Oloore, M. Gondal, A. Popoola and I. Popoola, *Carbon*, 2021, **173**, 1048–1058.

27 X. Yuan, X. Jiang, M. Cao, L. Chen, K. Nie, Y. Zhang, Y. Xu, X. Sun and Q. Zhang, *Nano Res.*, 2019, **12**, 429–436.

28 S. Sarkar, S. Ramarao, T. Das, R. Das, C. Vinod, S. Chakraborty and S. Peter, *ACS Catal.*, 2021, **11**(2), 800–808.

29 M. Choi, C. Ahn, H. Lee, J. Kim, S. Oh, W. Hwang, S. Yang, O. Kim, I. Choi, Y. Sung, Y. Cho, C. Rhee and W. Shin, *Appl. Catal., B*, 2019, **253**, 187–195.

30 Y. Feng, Q. Shao, F. Lv, L. Bu, J. Guo, S. Guo and X. Huang, *Adv. Sci.*, 2020, **7**, 1800178.

31 M. Din, F. Saleem, B. Ni, Y. Yong and X. Wang, *Adv. Mater.*, 2017, **29**, 1604994.

32 Y. Qin, M. Luo, Y. Sun, C. Li, B. Huang, Y. Yang and S. Guo, *ACS Catal.*, 2018, **8**, 5581–5590.

33 Y. F. Wang and A. S. Hall, *ACS Energy Lett.*, 2020, **5**(1), 17–22.

34 X. X. Zhou, Y. Y. Zhang, Y. F. Shen, S. Q. Liu and Y. J. Zhang, *Chem. Soc. Rev.*, 2018, **47**, 2298–2321.

35 J. Barrio, M. Volokh and M. Shalom, *J. Mater. Chem. A*, 2020, **8**, 11075–11116.

36 Z. Zhu, H. Yin, Y. Wang, C. Chuang, L. Xing, M. Dong, Y. Lu, G. Casillas-Garcia, Y. Zheng, S. Chen, Y. Dou, P. Liu, Q. Cheng and H. Zhao, *Adv. Mater.*, 2020, **32**, 2004670.

37 W. Gu, M. Wu, J. Sun, J. Xu and T. Zhao, *J. Mater. Chem. A*, 2019, **7**, 20132–20138.

38 W. Li, Z. Sun, J. Yang, G. Huang and H. Zhu, *Energy Environ. Mater.*, 2021, **647**, 1326–1333.

39 M. Zhang, C. Lai, B. Li, D. Huang, G. Zeng, P. Xu, L. Qin, S. Liu, H. Yi, M. Li, C. Chu and Z. Chen, *J. Catal.*, 2019, **369**, 469–481.

40 Z. Sun, Y. Wang, L. Zhang, H. Wu, Y. Jin, Y. Li, Y. Shi, T. Zhu, H. Mao, J. Liu, C. Xiao and S. Ding, *Adv. Funct. Mater.*, 2020, **30**, 1910482.

41 M. Bosca, L. Pop, G. Borodi, P. Pascuta and E. Culea, *J. Alloys Compd.*, 2009, **479**, 579–582.

42 U. I. Kramm, I. Herrmann-Geppert, P. Bogdanoff and S. Fiechter, *J. Phys. Chem. C*, 2011, **115**, 23417–23427.

43 W. G. Liu, L. L. Zhang, X. Liu, X. Y. Liu, X. F. Yang, S. Miao, W. T. Wang, A. Q. Wang and T. Zhang, *J. Am. Chem. Soc.*, 2017, **139**, 10790–10798.

44 G. Abarca, M. Viera, C. Aliaga, J. F. Marco, W. Orellana, J. H. Zagal and F. Tasca, *J. Mater. Chem. A*, 2019, **7**, 24776–24783.

45 C. C. Yang, S. F. Zai, Y. T. Zhou, L. Du and Q. Jiang, *Adv. Funct. Mater.*, 2019, **29**, 1901949.

46 B. Li, S. Sasikala, D. Kim, J. Bak, I. Kim, E. Cho and S. Kim, *Nano Energy*, 2019, **56**, 524–530.

47 T. Shinagawa, A. Garcia-Esparza and K. Takanabe, *Sci. Rep.*, 2015, **5**, 13801.

48 Q. Li, W. Chen, H. Xiao, Y. Gong, Z. Li, L. Zheng, X. Zheng, W. Yan, W. Cheong, R. Shen, N. Fu, L. Gu, Z. Zhuang, C. Chen, D. Wang, Q. Peng, J. Li and Y. Li, *Adv. Mater.*, 2018, **30**, 1800588.

49 C. X. Zhao, B. Q. Li, J. N. Liu and Q. Zhang, *Angew. Chem., Int. Ed.*, 2021, **60**, 4448.

50 D. Chen, R. Lu, Z. Pu, J. Zhu, H. Li, F. Liu, S. Hu, X. Luo, J. Wu, Y. Zhao and S. Mu, *Appl. Catal., B*, 2020, **279**, 119396.

51 Y. Chen, S. Ji, Y. Wang, J. Dong, W. Chen, Z. Li, R. Shen, L. Zheng, Z. Zhuang, D. Wang and Y. Li, *Angew. Chem., Int. Ed.*, 2017, **56**, 6937.

This journal is © The Royal Society of Chemistry 2022

J. Mater. Chem. A, 2022, **10**, 664–671 | **671**